Impact of strain rate sensitivity on the identification of the material parameters scattering and on the formability of zinc sheet

Article *in* International Journal of Material Forming · December 2018

DOI: 10.1007/s12289-019-01479-2

CITATIONS
0

READS
75

6 authors, including:

Marc Milesi
Umicore
25 PUBLICATIONS **69** CITATIONS
SEE PROFILE

Christophe Pradille
MAT XPER
15 PUBLICATIONS **35** CITATIONS
SEE PROFILE

Ludovic Vitu
Université de Technologie de Belfort-Montbéliard
5 PUBLICATIONS **2** CITATIONS
SEE PROFILE

Nathalie Boudeau
Institut FEMTO-ST
63 PUBLICATIONS **286** CITATIONS
SEE PROFILE

Impact of strain rate sensitivity on the identification of the material parameters scattering and on the formability of zinc sheet

M. Milesi [1,*], J. Lecoq[2], C. Pradille[3], L. Vitu[4], N. Boudeau[5], P.-O. Bouchard [2]

[1] *VM Building Solutions, Les mercuriales, 40 rue Jean-Jaurès, 93176 Bagnolet Cedex, France*
[2] *MINES ParisTech, PSL Research University, CEMEF - Centre de mise en forme des matériaux, CNRS UMR 7635, CS 10207 rue Claude Daunesse, 06904 Sophia Antipolis Cedex, France*
[3] *MatXper, 19 traverse du Barri, 06560 Valbonne, France*
[4] *ICB UMR 630, CNRS, Univ. Bourgogne Franche-Comté, UTBM, F-90010 Belfort, France*
[5] *FEMTO-ST Institute, UBFC / CNRS-UMR6174 / UFC / ENSMM / UTBM, Department of Applied Mechanics, Besançon, France*

Abstract: The mechanical behavior of zinc alloys drastically depends on strain rate and temperature, which are not constant during forming processes. During the production of zinc sheets, the slight variations of the industrial equipment parameters induce different local thermomechanical conditions. These variations could be stemming from a non-homogeneous cooling during rolling process, or local segregation of alloys and so on …. The result of these differences entails a significant scattering of material parameters as shown in [1]. This paper tackles the scattering of material parameters through an adapted Norton-Hoff behavior law. Then, four parameters have been identified with a standard Generalized Reduced Gradient method (GRG). Moreover, an exhaustive analysis of the entire rolled coil has been carried out to differentiate the variation coming from the material from the one due to the process. This study also encompasses the influence of strain rate on the forming limit diagram and therefore on the calculation of the forming limit stress diagram.

Keywords: Scattering, Inverse Method, Behavior Law, Forming Limit Stress Diagram

Introduction

Zinc alloys are commonly formed for building applications like pipes, gutters and facades. They are generally produced by continuous or semi continuous casting and rolling processes, which induce a very strong oriented structure, in addition to its intrinsic anisotropic hexagonal structure as discussed in [2]. An intermetallic phase with titanium alloy $TiZn_{16}$, inherited from the casting process, contributes to increase the anisotropy due to their stinger elongated forms as shown in [3]. Zinc alloys are highly

*Corresponding Author:
Phone: +33 4 93 95 74 43
Email: marc.milesi@vmzinc.com

dependent on temperature and strain rate, which trigger some formability changes as demonstrated by [4]. The law used by [5] fits correctly the experimental configurations for which stress-strain curves were obtained. Different strain rates and temperatures were tested in three directions with respect to the rolling direction (0°, 45° and 90°). A Norton-Hoff law with a temperature dependency given by an Arrhenius component, was proposed to describe the material behavior. However, to quantify the scattering for each material parameters, a simplified Swift law was initially studied in [1]. The choice of such a law is justified if experimental test configurations are the same, such as those practiced in the quality process developed in an industrial environment. For zinc, the standardization process implies only one strain rate condition for tensile test. Then, a Swift law is sufficient to identify the material behavior. The form of the equation used in [1] is given by:

$$\bar{\sigma} = K_{SWIFT}(\theta)(\varepsilon_0 + \bar{\varepsilon})^{n_{SWIFT}(\theta)} \quad (1)$$

where $\bar{\sigma}$ is the equivalent stress, $K_{SWIFT}(\theta)$ is the strength coefficient depending on the θ orientation with respect to the rolling direction, ε_0 the initial plastic strain set as a constant (fixed to 0.002), $\bar{\varepsilon}$ is the equivalent strain and $n_{SWIFT}(\theta)$ is the anisotropic hardening coefficient. The ε_0 was fixed to simplify the identification method by considering only two parameters. The convergence of the identification method is faster. In the same paper, the concept of scattering clouds and scattering domains to define statistical drawings restrained in the elliptical limits were presented. The method applied for calculating the minimum covering ellipse which encompasses all experimental data is the method proposed by [6]. The statistical drawings, following a Gaussian distribution, are described in [7].

In the present work, due to the K_{SWIFT} and n_{SWIFT} parameters dependencies to strain rate, an adapted form of the Norton-Hoff behavior law was proposed and identified. The standard behavior law is given by:

$$\bar{\sigma} = K_{NH}(\theta)(\bar{\varepsilon} + \varepsilon_0)^{n_{SWIFT}(\theta)}\dot{\bar{\varepsilon}}^{m(\theta)} \quad (2)$$

The difference with Eq. 1 is the explicit dependence of the equivalent strain rate $\dot{\bar{\varepsilon}}$ on $m(\theta)$, the strain rate sensitivity. To address the overall strain rate dependency, K_{SWIFT} and n_{SWIFT} parameters could be strain rate dependent parameters. K_{SWIFT} may be think as a strength coefficient parameter depending

both on orientation and strain rate, i.e. $K_{SWIFT} = K_{SWIFT}(\theta, \dot{\bar{\varepsilon}}) = K_{NH}(\theta)\dot{\bar{\varepsilon}}^{m(\theta)}$. However, an adapted form is needed to consider the dependency of the hardening coefficient on strain rate (i.e. $n_{SWIFT} = n_{SWIFT}(\theta, \dot{\bar{\varepsilon}})$). The goal is then to determine a relevant procedure to obtain precisely the most fitted material parameters.

The following part of this paper will describe the experimental set-up used to determine the statistical data stemming from different experimental tests. To assess the role of strain rate on the material parameters identification of the behavior law, different experimental set-ups related to tensile tests were used. Aftermath, experimental tests were enlarged to consider the entire formability characteristics of the material. The goal was to obtain the entire forming limit diagram to gauge the assessed loss of formability of the material for different loading conditions, especially in the expansive domain close to numerous industrial processes. In the second part, the identification procedure and the forming limit diagram will be presented and discussed.

The objective of this work is to improve more precisely the understanding of the complex behavior of zinc alloys. It is also important to assess precisely the scattering of material parameters to optimize the supply chain and adapt the formability of raw material batches for forming processes. This is the reason why experimental tests were performed for an entire primary coil formed by continuous rolling process.

1 Experimental set-up

The material sampling was performed directly during the cutting process, after the last pass of the rolling process. 10 sheets, with a surface of 1×1 m² and a thickness of 0.65 mm, were cut in the beginning of the primary coil, 10 other sheets were cut in the middle of the primary coil and 10 last ones, at the end. Each sheet was cut in 9 areas as schematized in Fig. 1. For each area of the different sheets, one flange (300×300 mm²) can be cut or 3 tensile test pre-forms (250×20 mm²) as described in Fig. 1. The sampling was precisely performed to reference the scattering along the primary coil.

The formability of zinc was studied with the forming limit diagram (FLD) proposed by [8]. The "negative" part of the FLD (i.e. minor strain < 0) was only determined by tensile tests. The positive part of the FLD was obtained with hydrostatic bulge tests, as described, for example, by [9]. Regarding

tensile tests, four velocities were tested in order to enlarge the studied domain: 0.45 mm/s, 10 mm/s, 100 mm/s and 300 mm/s (in terms of strain rate, 0.008 s^{-1}, 0.15 s^{-1}, 1.5 s^{-1} and 4.5 s^{-1}). 972 tensile tests were performed to obtain a representative scattering all along the entire coil.

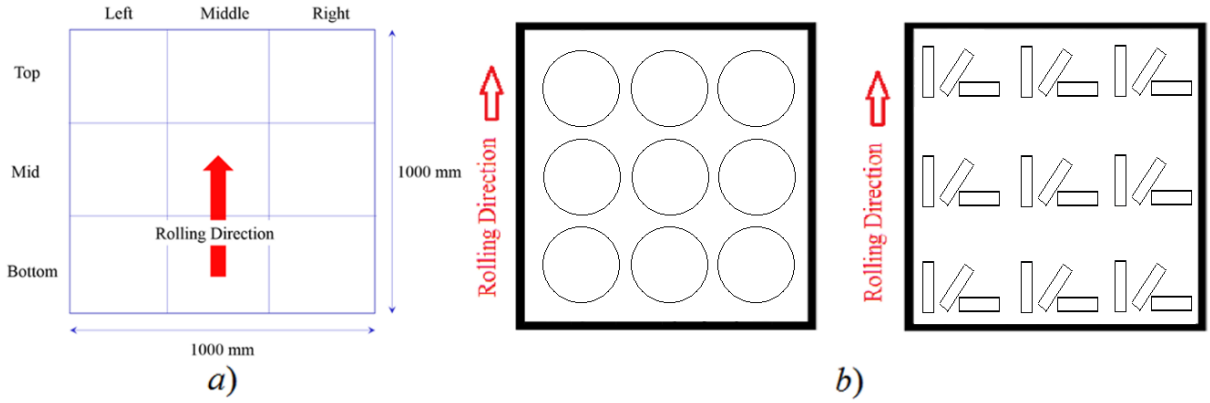

FIGURE 1: *a*) Sampling of each zinc sheet and *b*) Scheme of cut samples in a zinc sheet for bulge and tensile tests

Two kinds of tensile machines were used. For the lower velocities of the crosshead (0.45 mm/s and 10 mm/s), the tensile machine used was an Instron 1120 (10kN). For the higher velocities (100 and 300 mm/s), the tensile machine used was a Dartec HA 250 (50 kN). A commercial system of digital image correlation VIC3D (correlated solutions) was used to analyze the tensile tests. Two different systems were used during these tests:

- a stereo-correlation system with 2 cameras (AVT Pike with 50 mm objectives Schneider Kreuznach) was used for quasi static tensile test
- a medium speed camera from Vision research, a Miro 4x was used for the higher velocities. This camera records at 1,000 frames per second (fps) but images have a lower resolution

The evaluation of the displacement fields from which strains are calculated with Hencky assumption (which is the standard logarithmic strain used to calculate the true strain from experimental data) was performed with the commercial software VIC. The methodology proposed by [10] was applied to analyze the sensitivity of DIC parameters.

For bulge tests, the DIC commercial system with the two cameras was instrumented on a hydraulic bulge test machine. The expansive part of the FLD is described by changing different geometries of the matrix to change strain paths β (elliptic for $0 < \beta < 1$ and circular for $\beta = 1$). Three different matrixes were

used to impose different values of β. All tests were coupled with the DIC system, recording pictures during the test. FLDs were drawn by considering the deformation just before failure.

2 Swift Behavior law identification

Behavior law parameters were identified from tensile tests by the minimization of a cost function. The standard identification procedure is given by minimizing the following cost function:

$$f_c = \frac{1}{p}\sqrt{\sum_{i=1}^{p}\frac{\left(\sigma_i^{mod}-\sigma_i^{exp}\right)^2}{\left(\sigma_i^{exp}\right)^2}} \quad (3)$$

where p defines the number of experimental measurement points, σ_i^{mod} and σ_i^{exp} are, respectively, the true stress calculated with the theoretical behavior law and the experimental stress. The algorithm applied to converge towards the minimum is a Generalized Reduced Gradient (GRG) method, used by [11], with 100 iterations and a precision of 10^{-6} between the last cost function value and the previous one after one iteration. For each parameter, the GRG method identification converges rapidly towards the global minimum for the initial set of parameters when two variables are considered (as shown in [1]). From tensile test curves, the identification method GRG gives the two parameters of the Swift behavior law given by Eq. 1 (strength coefficient K_{SWIFT} and hardening coefficient n_{SWIFT}). Fig. 2 describes an example of the identification of different experimental curves. The equivalent stress-strain curves are calculated from a Von Mises yield criterion. In this approach, the anisotropy is only considered in the behavior law and not in the definition of the yield stress. The parameters of the Swift law were identified by considering the part of the curve from the yield stress to the ultimate tensile strength. As shown, the tendency is correctly fitted.

In the following, it has been decided to identify the couple of (K_{swift}; n_{Swift}) parameters for two different velocities. Dependence to strain rate with an adapted Norton-Hoff law will be discussed in the next section. Fig. 3 shows the variation of the strength coefficient all along the coil for the two-extreme strain rates (0.008 s^{-1} and 4.5 s^{-1}). Due to the difficulty in analyzing the results at high velocities (because the equipment used is less accurate in terms of image resolution), tensile tests are less numerous at 4.5 s^{-1}. For each orientation with respect to the rolling direction and for each velocity, the scattering depending

on the position of the samples on the sheet is very restrained. The K_{SWIFT} values highly depend on strain rate, which induces an increase of more than 80 % as seen in Tab. 1. It can be noticed that the difference between 45° and 90° configurations is reduced for 4.5 s^{-1}.

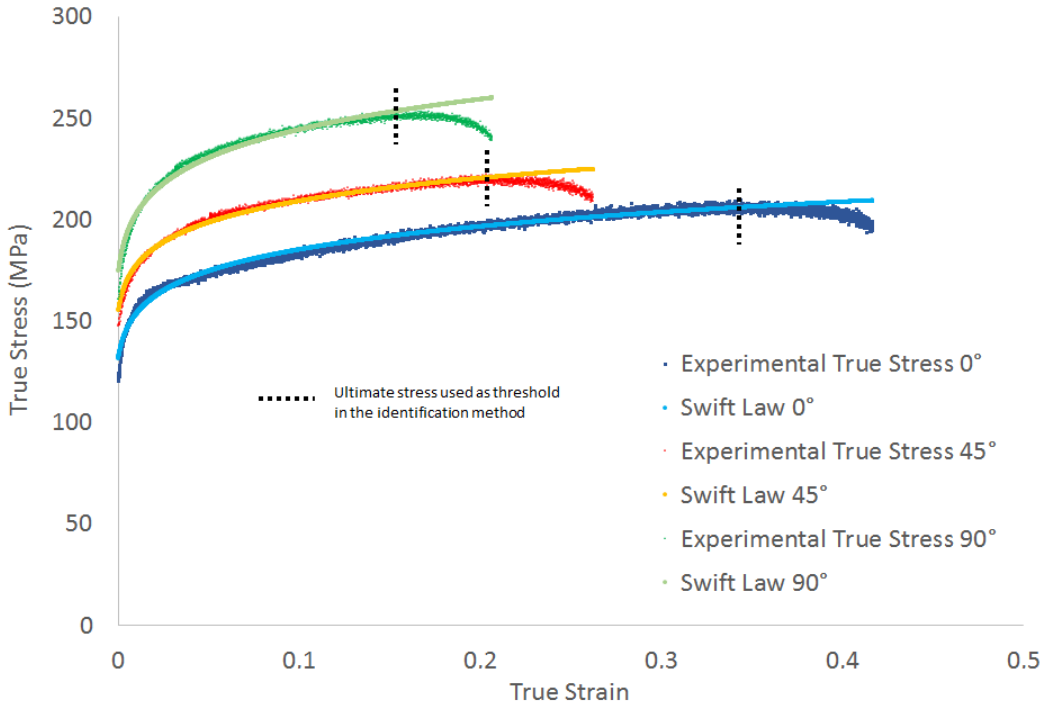

FIGURE 2: Example of the identification of the K_{swift} and n_{Swift} parameters from the true stress-strain curves for three directions with respect to the rolling direction (0°, 45° and 90°)

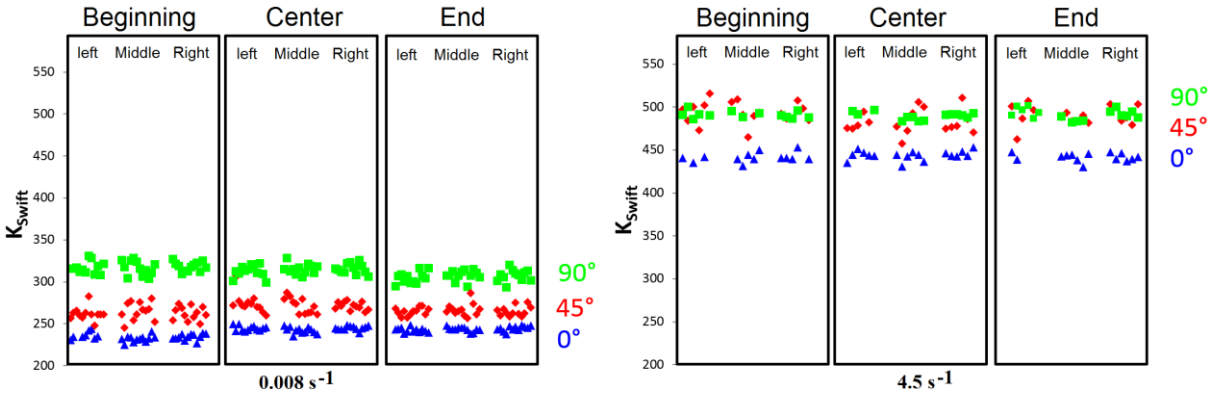

FIGURE 3: Variation of the K_{SWIFT} parameters (MPa) all along the entire coil (at the beginning, the center and the end) in the middle and the edges in the width: 0.008 s^{-1} and 4.5 s^{-1}

Stain rate (s^{-1})		**0°**	**45°**	**90°**
0.008	Mean value	240.5	267	312.7
	Standard deviation	5.1	5.7	5.6
4.5	Mean value	442.2	489.4	490.8
	Standard deviation	3.4	10.6	4.3

TABLE 1: Mean values and standard deviations of the K_{SWIFT} parameters (MPa) along the entire coil

Fig. 4 shows the variation of the hardening coefficients all along the coil for the two-extreme strain rates (0.008 s^{-1} and 4.5 s^{-1}). The conclusion is the same as previously discussed for the K_{SWIFT} parameter. The scattering does not depend on the position on the sheet or on the coil. However, the n_{SWIFT} values strongly depend on the strain rate. Indeed, for the low strain rate, the hardening coefficient n_{SWIFT} is quite equal for the different orientations whereas the more the strain rate increases, the more the coefficients n_{SWIFT} increase. Tab. 2 sums up the values of the hardening coefficients along the entire sheet.

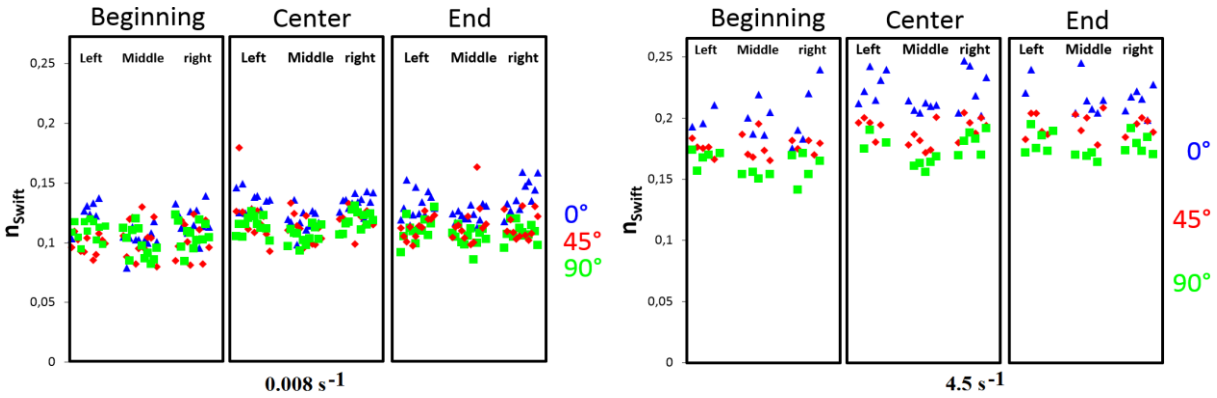

FIGURE 4: Variation of the n_{SWIFT} parameters all along the entire coil (at the beginning, the center and the end) in the middle and the edges in the width: 0.008 s^{-1} and 4.5 s^{-1}

Stain rate (s^{-1})		0°	45°	90°
0.008	Mean value	0.125	0.111	0.109
	Standard deviation	0.0118	0.0097	0.0072
4.5	Mean value	0.213	0.187	0.1707
	Standard deviation	0.0141	0.0092	0.0106

TABLE 2: Mean values and standard deviations of the n_{SWIFT} parameters along the entire coil

3 Adapted Norton-Hoff Behavior law

Due to the dependency of the strength coefficient K_{SWIFT} and the hardening coefficient n_{SWIFT} on strain rate and on the orientation with respect to the rolling direction, a new identification is necessary. The identification scheme can be summed up in Fig. 5. K_{SWIFT} and n_{SWIFT} were split by considering two more parameters for each of them: $K_{NH}, m,\ A$ and n_{NH}. K_{NH} is the strength coefficient independent of strain rate and m, a parameter relating to the strain rate sensitivity of the strength. n_{NH} is named hardening coefficient of the adapted Norton-Hoff behavior law and A, is the strain rate dependency of the hardening.

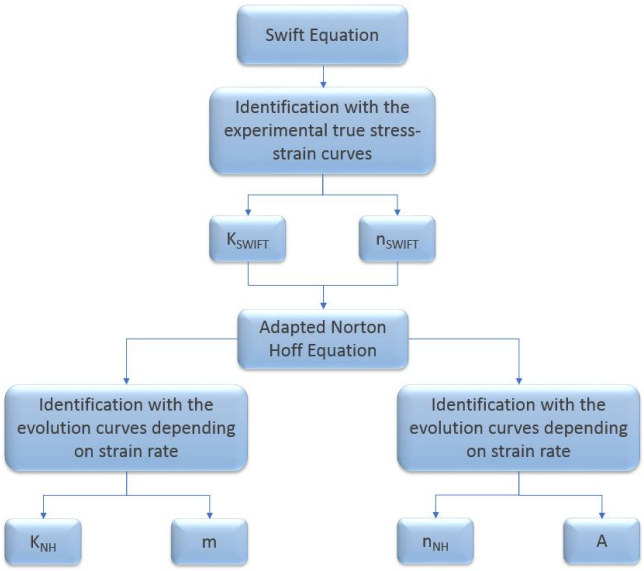

FIGURE 5: Identification scheme to determine the adapted Norton-Hoff behavior law

The most fitted equation for K_{SWIFT} is an exponential. Consequently, the evolution of the strength coefficient K_{SWIFT} was decomposed by a new strength coefficient K_{NH} independent of strain rate, plus a term depending on strain rate:

$$K_{SWIFT} = K_{NH}\dot{\varepsilon}^{m(\theta)} \tag{4}$$

As shown in Fig. 6, this decomposition of the K_{SWIFT} parameter gives Pearson coefficients R^2 very close to 1 which validates this approximation.

For the n_{SWIFT} coefficient, the simplest equation with two parameters given the best Pearson coefficients (compared to an exponential, linear or a quadratic equation), as shown in Fig. 7, is:

$$n_{SWIFT} = n_{NH} + A\ ln(\dot{\varepsilon}) \tag{5}$$

The choice of such two parameters equation is a compromise between rapidity of the identification method and precision, with Pearson coefficients more than 0.6. The suggested model for the n_{SWIFT} parameter has also the advantage to converge towards the minimum global value of the cost function with few incrementations. However, the modeling effort is a first attempt towards describing the observed behavior (a precise modeling goes beyond the scope of the paper and will be the object of future works). Physically, n_{NH} is not the standard hardening coefficient but defines a part of the standard definition introduced by Hollomon.

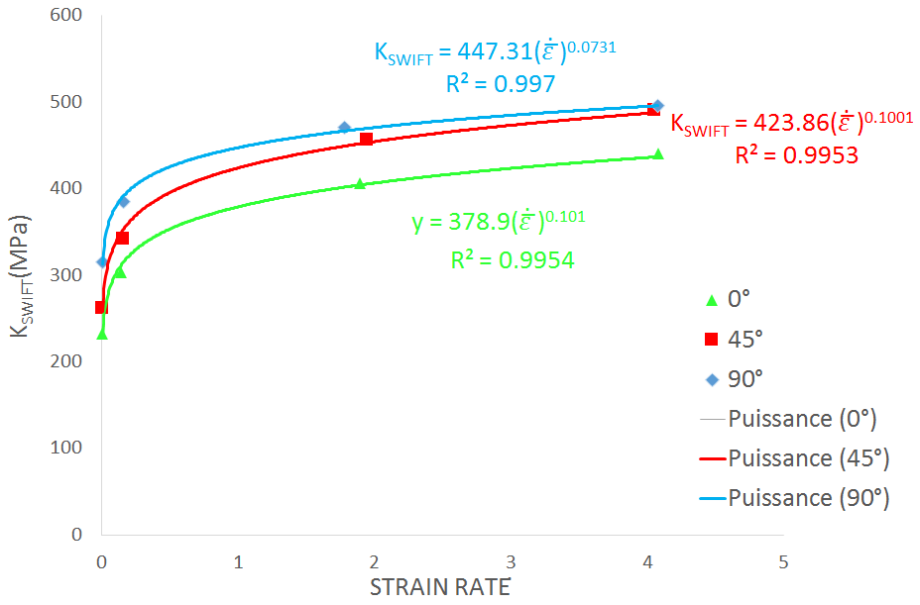

FIGURE 6: Example of the evolution of the strength coefficient compared to the strain rate and identification with an exponential equation depending on strain rate

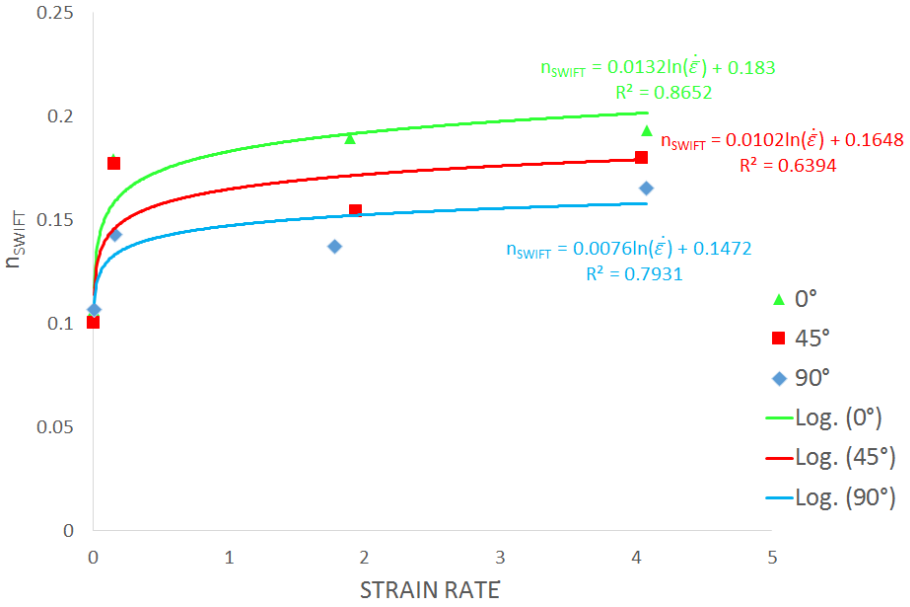

FIGURE 7: Example of the evolution of the hardening coefficient compared to the strain rate and identification of the hardening coefficient with a logarithmic equation depending on strain rate

The final form of the behavior law is then given by:

$$\bar{\sigma} = K_{NH}(\theta)(\bar{\varepsilon} + \varepsilon_0)^{n_{NH}(\theta)+A(\theta)\, ln\, \dot{\bar{\varepsilon}}}\, \dot{\bar{\varepsilon}}^{m(\theta)} \tag{6}$$

All material parameters depend on the orientation with respect to the rolling direction θ. As described by [1], the unicity of all parameters can be verified if the equation is only composed by two parameters, which is the case of the Eq. (4) and Eq. (5). As described in the experimental set-up, four velocities have

been tested, which implies that the identification method can be applied. Figs. 8 *a*), 8 *b*), 8 *c*) and 8 *d*) show visually the variation of the four identified parameters. The scattering of the four parameters all along the coil and the width is similar and, as a conclusion, does not depend on the position of the sampling. Tab. 3 sums up all values of the 4 parameters averaged all along the coil.

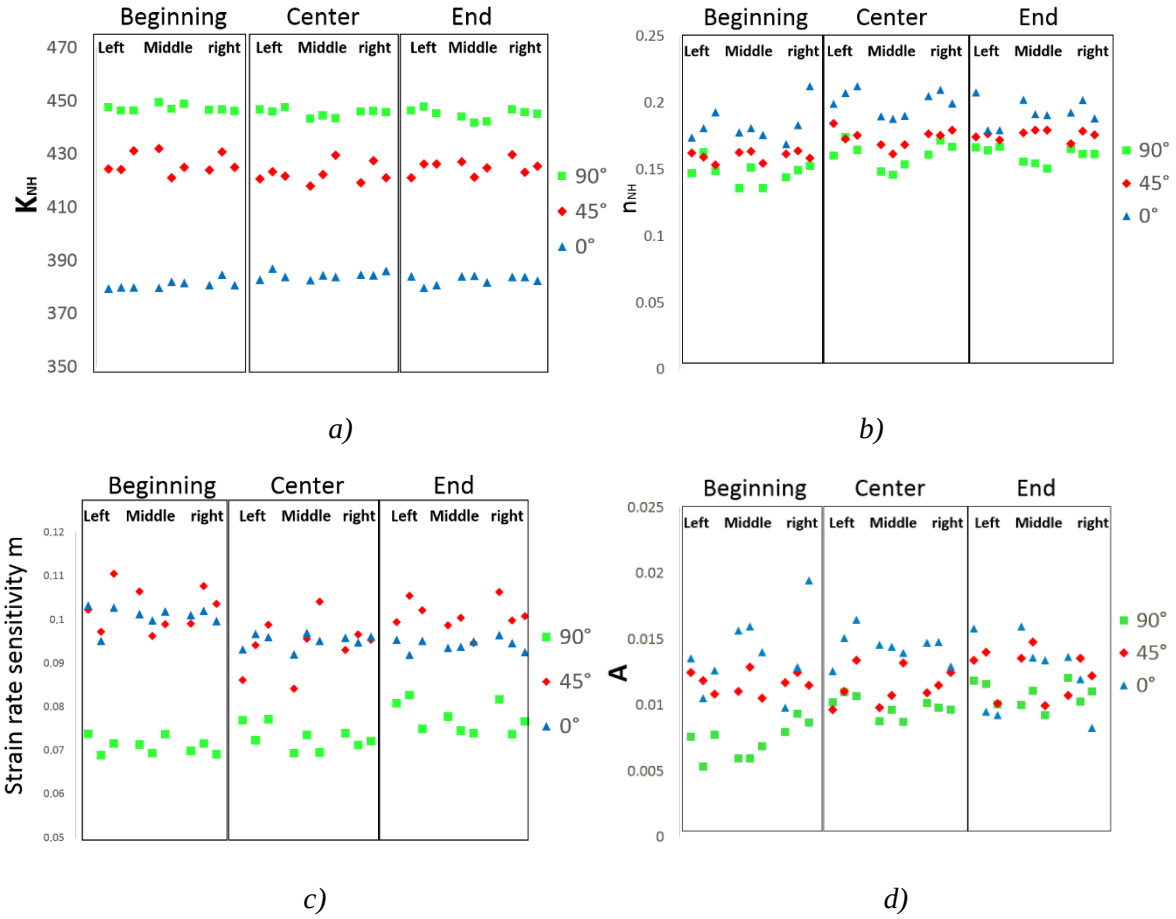

FIGURE 8: Variation of the four material parameters of the adapted Norton-Hoff law all along the entire coil (at the beginning, the center and the end) in the middle and the edges in the width: *a*) strength coefficient K_{NH}; b) hardening coefficient n_{NH}; *c*) strain rate sensitivity *m* and *d*) strain rate dependency *A*

		0°	**45°**	**90°**
K_{NH}	Mean value	382.69	424.65	445.85
	Standard deviation	2.08	3.76	1.79
n_{NH}	Mean value	0.19	0.17	0.157
	Standard deviation	0.013	0.009	0.0101
A	Mean value	0.0135	0.0119	0.009
	Standard deviation	0.0025	0.0014	0.0018
m	Mean value	0.097	0.1	0.074
	Standard deviation	0.0035	0.006	0.004

TABLE 3: Identification of the adapted Norton-Hoff material parameters

The correlation between each parameter has also been calculated to assess their link. Tab. 4 sums up the average of all correlation coefficients in the three directions and as shown, no significant correlation can be noticed.

	n_{NH}	K_{NH}	A	m
n_{NH}	1	0.036	0.476	-0.137
K_{NH}		1	-0.015	-0.194
A			1	0.432
m				1

TABLE 4: Correlations between the material parameters identified by the GRG method

Fig. 9 shows the 3D representation of K_{NH}, n_{NH}, m clouds (averaged values) and the ellipsoidal domain defined in [6], which is an extension of the method presented in [1]. It can be noted that the m coefficient determined in the 45° orientation with respect to the rolling direction is more scattered. Such ellipsoidal domains are employed to establish statistical drawings in order to calculate the critical stress defined in [1]. Indeed, to calculate the Scattering Forming Limit Stress Diagram (SFLSD), it is necessary to use the statistical equivalent strains calculated from the FLD and randomly associated them to the behavior law parameters and therefore obtain the critical stress. Then, the statistical bands describing the scattering of the critical stresses are used to define a criterion fitted for numerical calculations as demonstrated by [1]. This criterion is based on the probability density function (PDF) calculated from the numerical local stress for each mesh element compared to the experimental Gaussian distribution. The PDF is defined by:

$$PDF(\bar{\sigma}(\beta)) = \frac{1}{\bar{\sigma}_{SD}\sqrt{2\pi}} e^{-\frac{(\bar{\sigma}-\bar{\sigma}_{MEAN})^2}{2(\bar{\sigma}_{SD})^2}} \quad (7)$$

where $\bar{\sigma}(\beta)$ means the numerical equivalent stress for each strain path β, $\bar{\sigma}_{MEAN}$ and $\bar{\sigma}_{SD}$ are respectively the mean and the standard deviation of the experimental critical equivalent stress for each strain path. During the simulation, the PDF is summed for each step to determine the CDF (Cumulative Density Function) which gives the probability of the defects occurrence.

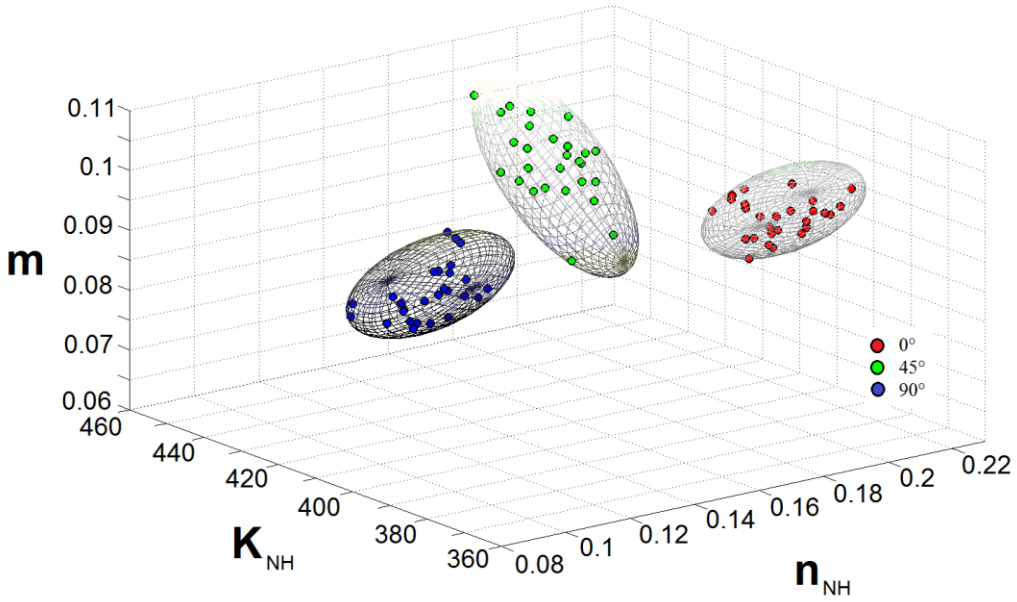

FIGURE 9: Scattering ellipsoidal domains or ellipsoidal clouds defined by the strength coefficient K_{NH}, the hardening coefficient n_{NH} and the strain rate sensitivity coefficient m

Numerically, the identification of material parameters can be used by averaging all data and by considering different configurations. As explained in [1], to apply the statistical data, it is important to consider the normal value (or also called averaged value) of each parameter. For example, the minimum normal value of K_{NH} is an average in the three directions as defined by the following equation:

$$\overline{K}_{NH\ min} = \frac{K^{0°}_{NH\ min} + 2K^{45°}_{NH\ min} + K^{90°}_{NH\ min}}{4} \quad (8)$$

Then, for the simulation, several configurations can be tested by crossing the minimum values, with the mean values and the maximum values. With 4 material parameters, the numerical plan is given by 81 numerical tests to obtain all configurations.

4 Forming Limit Diagram

To complete the FLD, Fig. 10 relates all data obtained from the tensile tests (on the left part of the chart) and the bulge tests (on the right part) by reporting the major strain (ε_1) and minor strain (ε_2) obtained by DIC system.

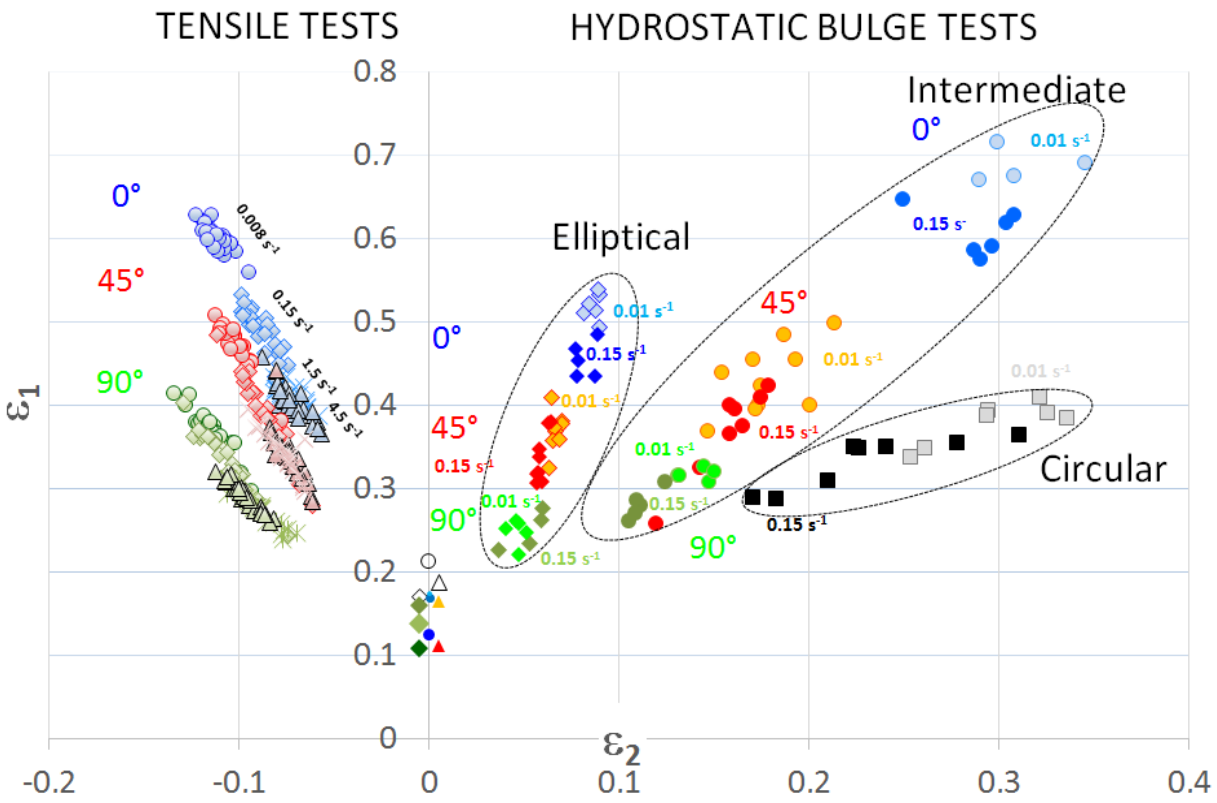

FIGURE 10: Influence of strain rate on the experimental forming limit diagram (FLD)

To determine the positive strain quadrant of the FLD, the equipment used is a hydraulic bulge test apparatus described by [9]. Three kinds of elliptic masks define three theoretical strain paths given by $\beta = \frac{\varepsilon_2}{\varepsilon_1} = \frac{minor\ strain}{major\ strain}$; β = 0.2, 0.5 and 1. β = 1 is the hemispheric mask defining the same deformation in the direction of the major strain and the minor strain. All data are given in Tabs. 5 and 6. Strain rates obtained for bulge tests are equivalent to the lower strain rates used for tensile tests (0.008 s^{-1} and 0.15 s^{-1}) by considering an averaged value of the strain rate. For example, in Fig. 11, the strain rate evolution (calculated from the variation of the equivalent strain for each time step obtained from DIC analyses) is plotted as a function of the time for a flow of 2 cm^3/min. The strain rate is not constant because the velocity is controlled by the flow speed of the liquid to insure pressure on the flange. Then, the strain rate value is assessed from an averaged value during the entire test. For bulge tests, the velocity depends on the form of the mask. The lower the strain path (β) is, the higher the strain rate is (Fig. 11). For each strain path, the flow speed of 2 cm^3/min gives a strain rate around 0.01 s^{-1}. The strain rate is close to 0.15 s^{-1} for a flow speed equals to 18 cm^3/min for β = 0.2, 29 cm^3/min for β = 0.5 and 50 cm^3/min for β = 1). The equivalent strain rates were verified by means of DIC system.

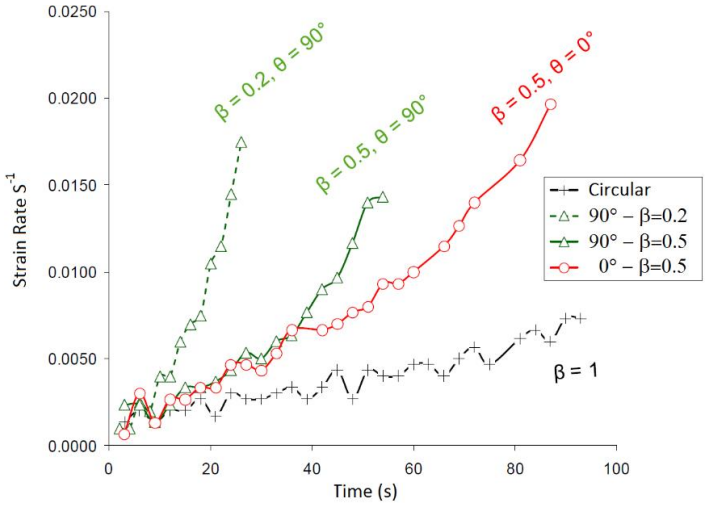

FIGURE 11: Strain rates obtained during bulge tests for 2 cm^3/min

	Tensile tests				Bulge test - Elliptical		Bulge test - Intermediate		Bulge test - Circular	
Strain rate (s^{-1})	0.008	0.15	1.5	4.5	0.01	0.15	0.01	0.15	0.01	0.15
0°	0.6	0.49	0.41	0.4	0.52	0.46	0.69	0.61		
45°	0.47	0.38	0.35	0.34	0.37	0.34	0.43	0.37	0.38	0.33
90°	0.37	0.33	0.28	0.29	0.25	0.25	0.32	0.28		

TABLE 5: Values of the major strain ε_1

	Tensile tests				Bulge test - Elliptical		Bulge test - Intermediate		Bulge test - Circular	
Strain rate (s^{-1})	0.008	0.15	1.5	4.5	0.01	0.15	0.01	0.15	0.01	0.15
0°	-0.11	-0.09	-0.07	-0.07	0.087	0.007	0.31	0.29		
45°	-0.1	-0.08	-0.07	-0.08	0.067	0.004	0.18	0.16	0.23	
90°	-0.11	-0.11	-0.09	-0.11	0.052	0.004	0.14	0.11		

TABLE 6: Values of the minor strain ε_2

As shown in Fig. 10, the Forming Limit Curves corresponding to the three directions (FLCs) are slightly impacted by strain rate. To underpin this point, Fig. 12 shows the centers of the elliptic domains. As shown, all data are located on the same curve. The centers of the elliptic domains are sensitive to the strain rate but the formability is in the same FLC because the variation is linear. It means that for each orientation with respect to the rolling direction, it exists one FLC to gather all data. However, the formability decreases as a function of strain rate. For or each orientation, the interpolation of all centers

with a line is excellent with Pearson coefficients close to 1. For the positive quadrant, the centers of the elliptic domains are dragged lower as shown in Fig. 13.

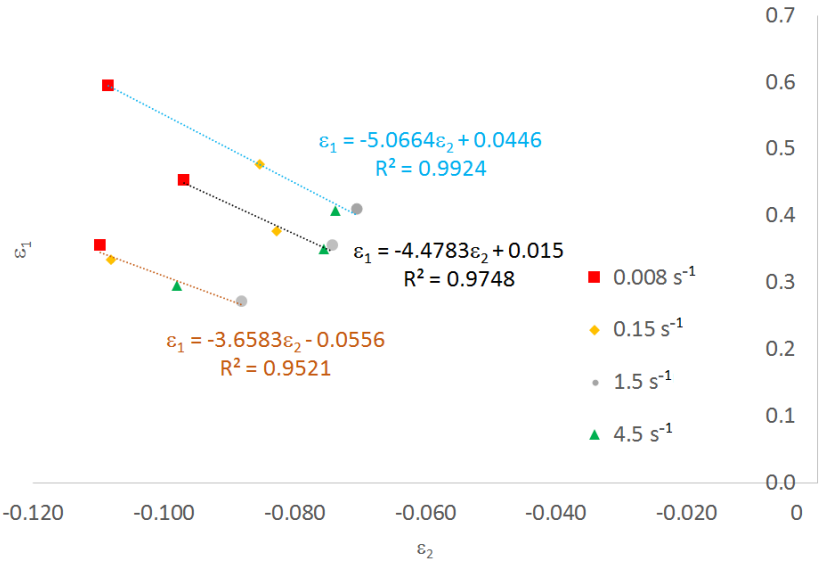

FIGURE 12: Centers of the elliptic domains related to the tensile tests in 0°, 45°, 90° directions

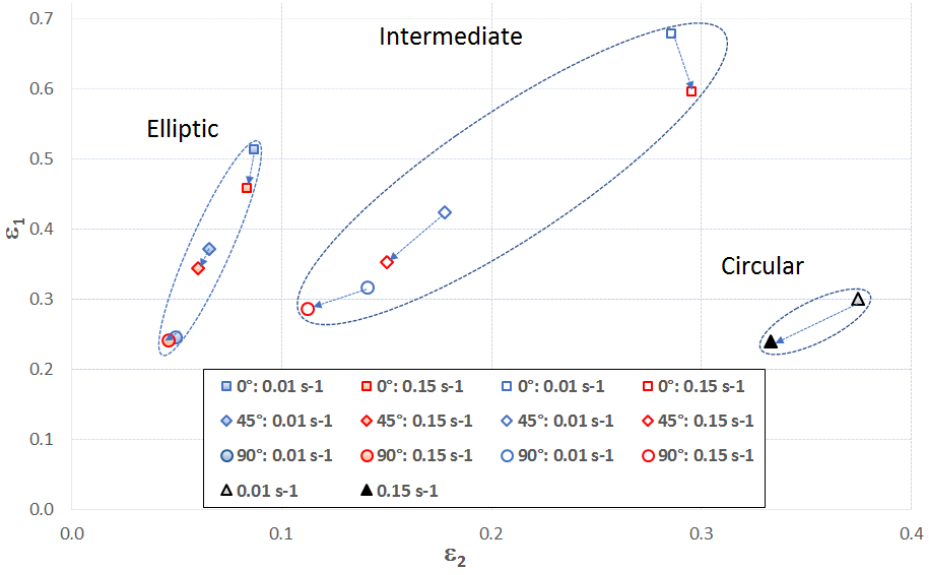

FIGURE 13: Centers of the elliptic domains related to the hydroforming tests in 0°, 45°, 90° directions

In Fig. 12, the slope is given by using the Lankford coefficient *r*:

$$\frac{\varepsilon_1}{\varepsilon_2} = -\frac{\varepsilon_3+\varepsilon_2}{\varepsilon_2} = -\frac{1+r}{r} \qquad (9)$$

Fig. 14 indicates the variation of *r* as a function of number of samples for all strain rates. In Fig. 15, values of *r* Lankford coefficients have been averaged to determine its dependence on strain rate. The slope of each approximate linear function underpins the non-significant dependence of *r* on strain rate.

This conclusion induces the results of the linear tendency noted for tensile tests in Fig. 12 because the slope is relatively constant.

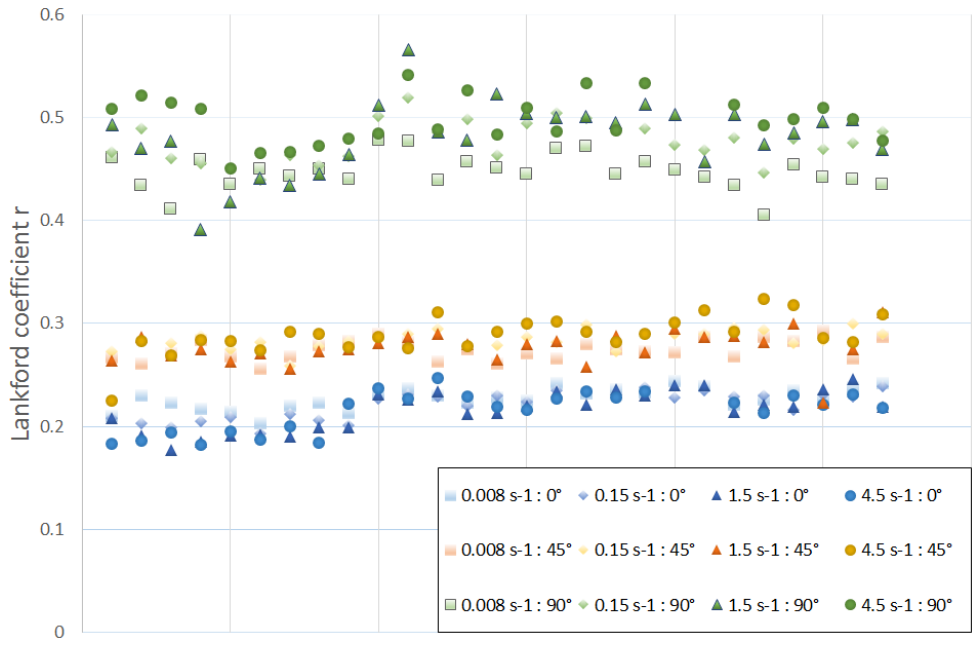

FIGURE 14: Variation of the Lankford coefficients as a function of strain rate for each sample

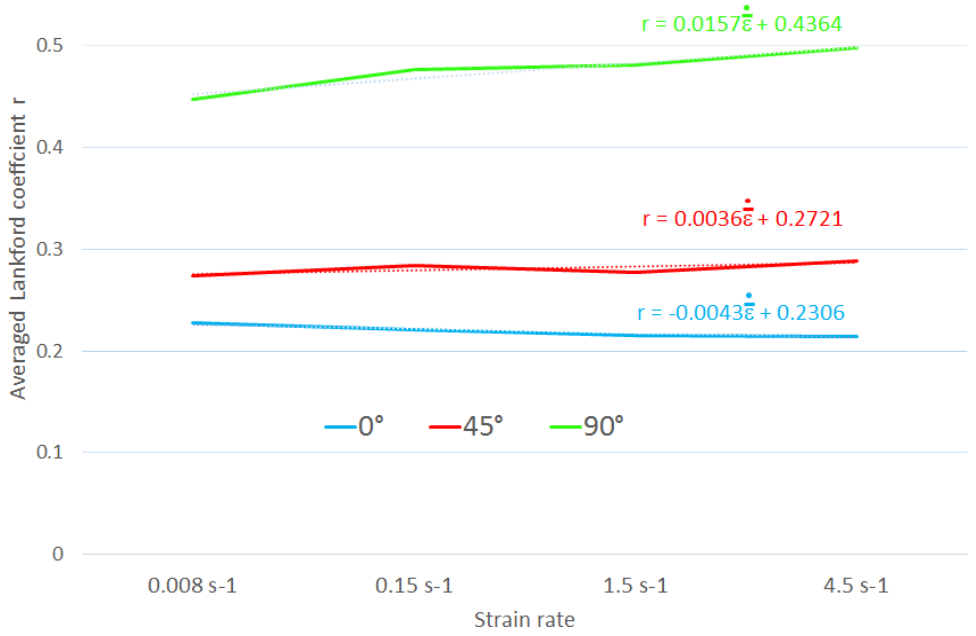

FIGURE 15: Mean values of the Lankford coefficients compared to the strain rate

In Figs. 16, 17 and 18, the minimum covering ellipses were calculated for each configuration from the scattering domains delimited by the Khachiyan algorithm [6]. All data related to the calculation of the elliptic domains are referenced in Tabs. 7 to 10.

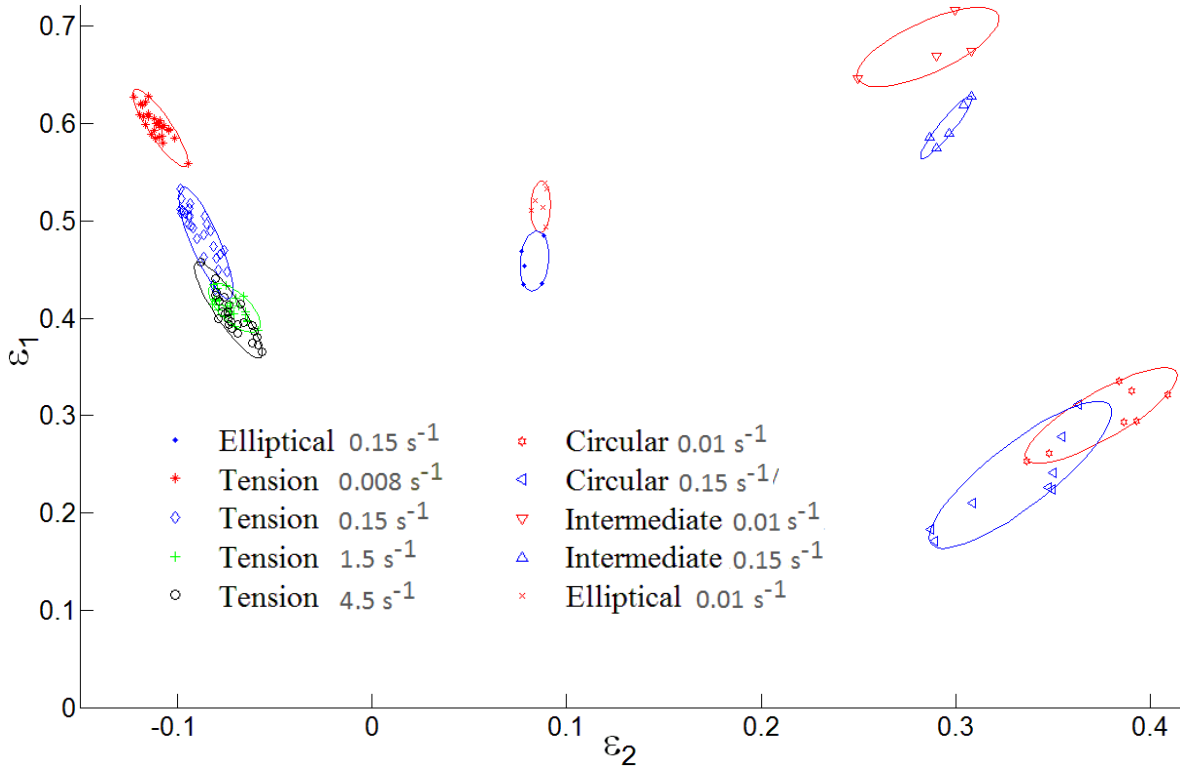

FIGURE 16: Minimum covering ellipses calculated in the rolling direction (i.e. 0°)

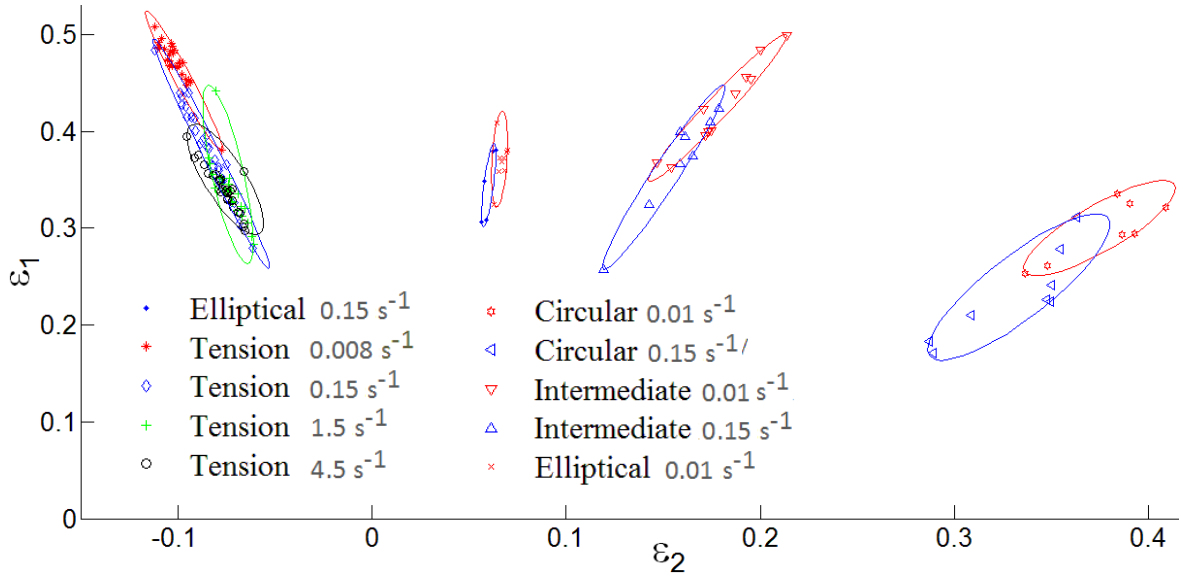

FIGURE 17: Minimum covering ellipses calculated in the diagonal direction compared to the rolling direction (i.e. 45°)

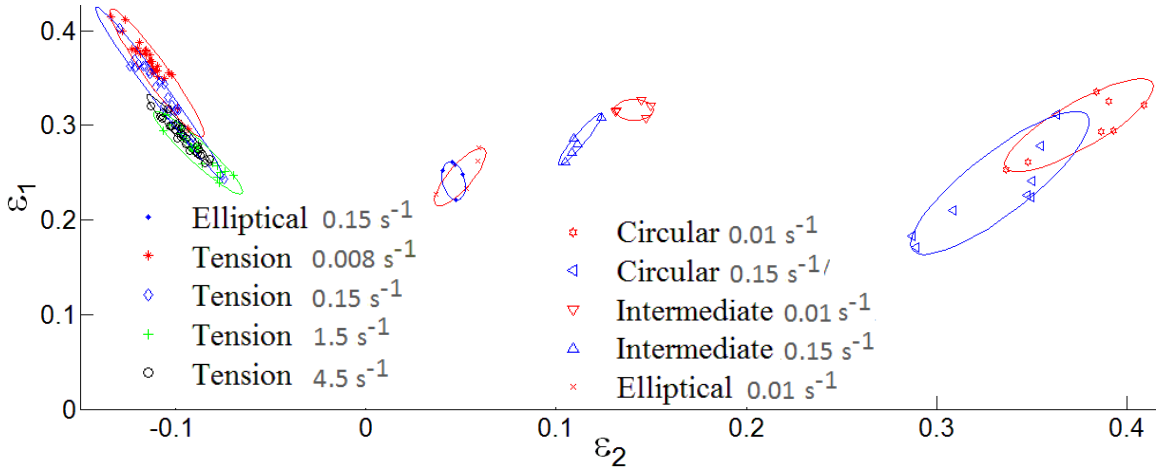

FIGURE 18: Minimum covering ellipses calculated in the transverse direction compared to the rolling direction (i.e. 90°)

Strain rate (s^{-1})	**0.008**			**0.15**			**1.5**			**4.5**		
	0°	45°	90°	0°	45°	90°	0°	45°	90°	0°	45°	90°
Center (ε_2)	-0.11	-0.097	-0.11	-0.09	-0.083	-0.11	-0.07	-0.07	-0.09	-0.07	-0.07	-0.1
Center (ε_1)	0.60	0.45	0.35	0.48	0.38	0.33	0.41	0.36	0.27	0.41	0.35	0.29
Angle of the major axis	17.5°	15.06°	19.4°	11.5°	14.04°	20.1°	22.3°	6.25°	27.3°	17.7°	15.8°	23.9°
Semi major axis	0.04	0.075	0.07	0.06	0.122	0.10	0.03	0.093	0.05	0.05	0.059	0.04
Semi minor axis	0.01	0.005	0.01	0.01	0.005	0.01	0.01	0.008	0.01	0.01	0.012	0.004

TABLE 7: Elliptic domains defined for tensile tests in 0°, 45° and 90° directions

Strain rate (s^{-1})	**0.01**			**0.15**		
	0°	45°	90°	0°	45°	90°
Center (ε_2)	0.09	0.066	0.05	0.08	0.060	0.05
Center (ε_1)	0.51	0.371	0.25	0.46	0.345	0.24
Angle of the major axis	-0.8°	-1.64°	-20.96°	-2.35°	-3.71°	5.31°
Semi major axis	0.03	0.05	0.03	0.03	0.043	0.02
Semi minor axis	0.005	0.004	0.01	0.01	0.003	0.01

TABLE 8: Elliptic domains defined for $\beta = 0.2$ in 0°, 45° and 90° directions

Strain rate (s^{-1})	**0.01**			**0.15**		
	0°	45°	90°	0°	45°	90°
Center (ε_2)	0.29	0.18	0.14	0.3	0.15	0.11
Center (ε_1)	0.68	0.42	0.32	0.6	0.35	0.29
Angle of the major axis	-40.66°	-24.74°	6.83°	-21.34°	-17.94°	-21.83°
Semi major axis	0.05	0.084	0.01	0.03	0.1	0.03
Semi minor axis	0.02	0.007	0.01	0.004	0.008	0.004

TABLE 9: Elliptic domains defined for $\beta = 0.5$ in 0°, 45° and 90° directions

Strain rate (s^{-1})	0.01	0.15
Center (ε_2)	0.3	0.24
Center (ε_1)	0.37	0.33
Angle of the major axis	-37.27°	-29.82°
Semi major axis	0.06	0.09
Semi minor axis	0.02	0.02

TABLE 10: Elliptic domains defined for $\beta = 1$ in 0°, 45° and 90° directions

5 Scattering Forming Limit Diagram and Scattering Forming Limit Stress Diagram

The determination of all scattering domains or also named cloud domains can be used to construct the statistical forming stress diagram. In [12], the authors demonstrated that such criteria were adapted to predict zinc formability. The method is described in [13] and extended in [1].

From the major and the minor strains of the FLD, statistical equivalent strains are calculated and randomly associated to the identified parameters of the behavior law. The elliptic domains are applied to limit the numerical statistical drawings described by [7] with random selection carried out with the Mersenne Twister algorithm [14]. To calculate the transformation, it is necessary to define the center of the restricted elliptic domain, the angle, and the major and minor axes. The algorithm chosen to define the minimum covering ellipse enclosing a cloud of points ensued from the ellipsoid method published in [6]. The method constructs iteratively sequences of different ellipses by considering each point one by one. The iterative step is repeated until all values have been tested. The scattering forming limit diagrams are calculated after defining the scattering domains as shown in Figs.19.

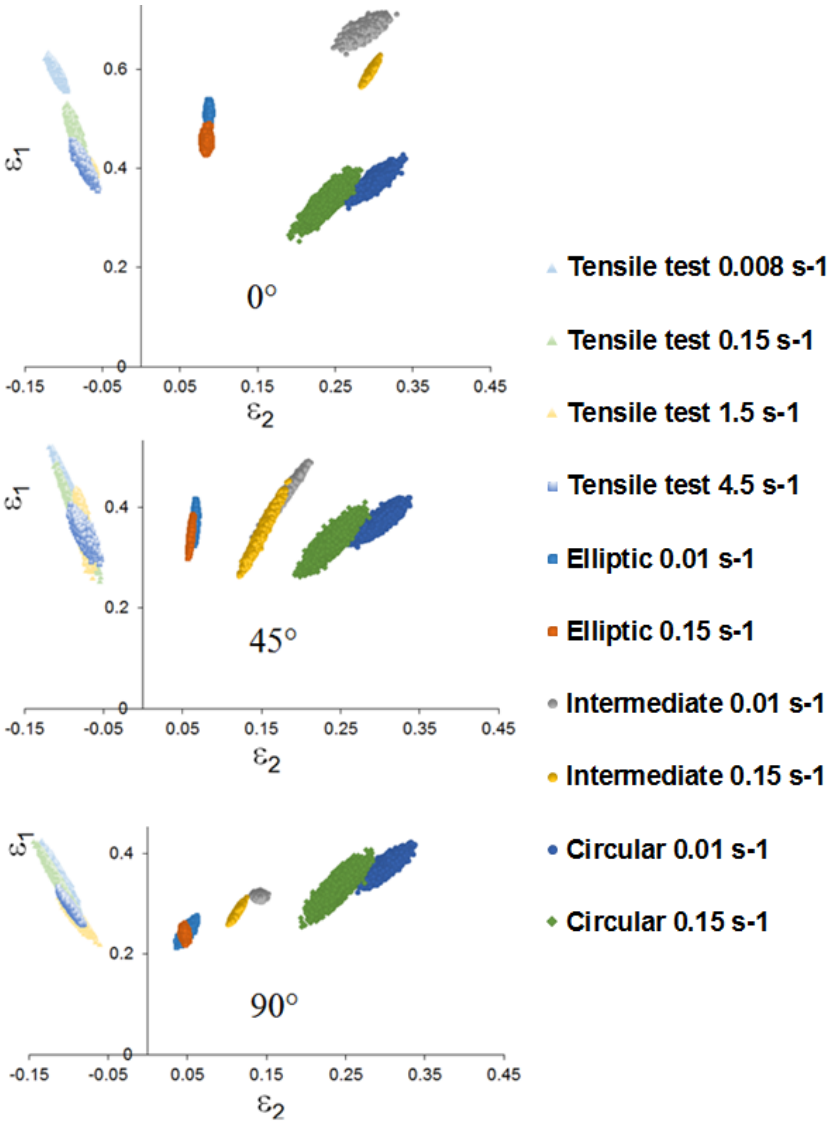

FIGURE 19: Statistical drawings restraining by elliptic Khachiyan domains defined by the minimum covering ellipse. SFLD in the 0°, 45° and 90° with respect to the rolling direction

In Figs. 20, all scattering domains are plotted, defining the Scattering Forming Limit Diagram (SFLD) for the three anisotropic directions.

From the SFLD, the equivalent strain, determined statistically, can be used in the behavior law. The four parameters of the behavior law are drawn statistically by following a Gaussian law. Then, the critical stresses calculated from the SFLD and the scattering behavior parameters of the behavior law define the Scattering Forming Limit Stress Diagram (SFLSD) plotted in Figs. 21. Each parameter is crossed randomly with a statistical equivalent strain obtained from the SFLD.

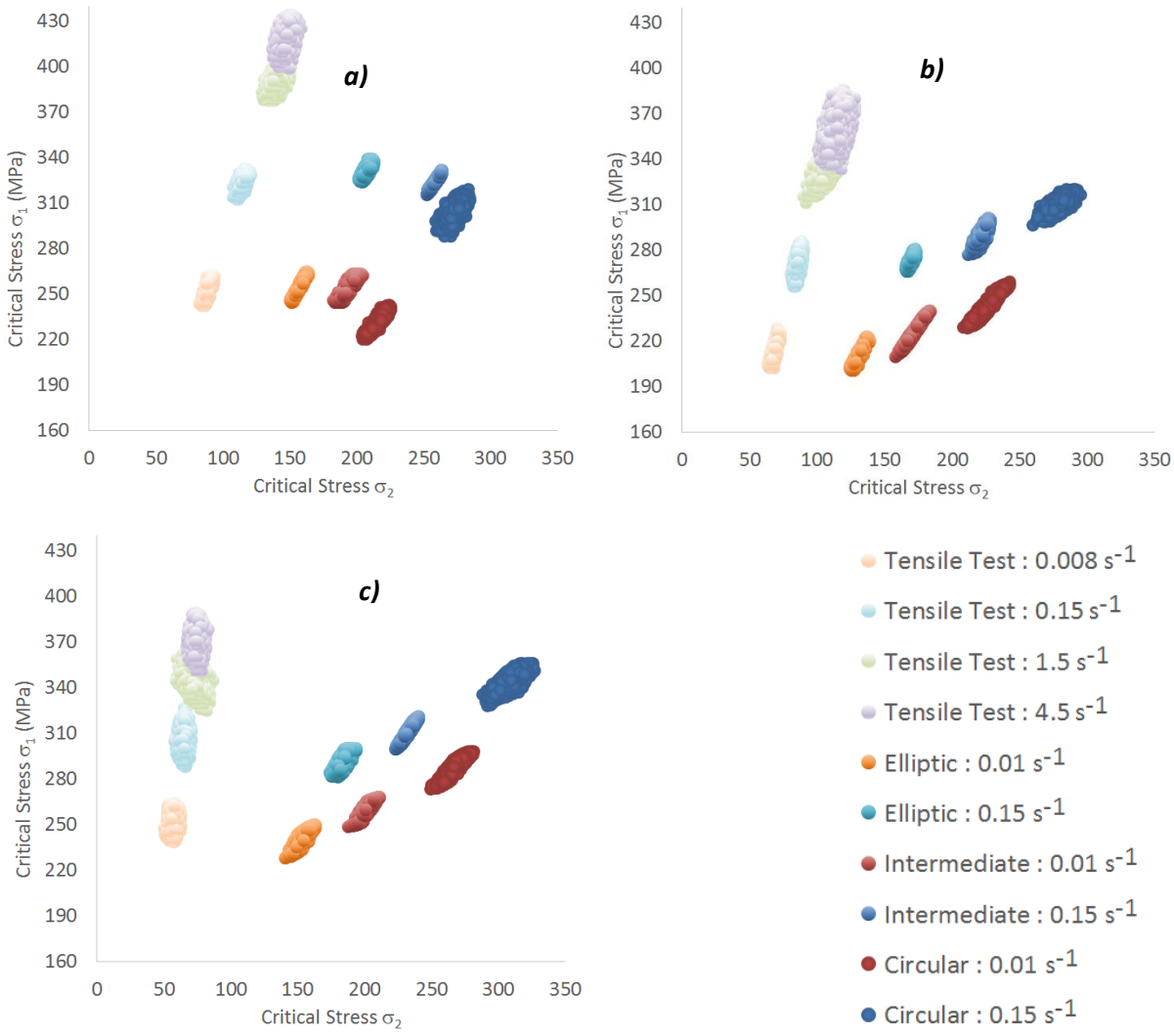

FIGURE 20: Scattering Forming Limit Stress Diagram (SFLSD) in the *a*) 0°; *b*) 45° and *c*) 90° directions

To generate the SFLSD, the adopted conversion from the SFLD is the same as described in [15]. The major stress σ_1 and the minor stress σ_2 are calculated from the stress path α and strain path β by the following equations:

$$\sigma_2 = \alpha\sigma_1 \tag{10}$$

α depends on the strain path as defined as following:

$$\alpha = \frac{1+2\beta}{2+\beta} \tag{11}$$

Finally, the major stress is defined by the following equation:

$$\sigma_1 = \frac{\bar{\sigma}}{\sqrt{1+\alpha^2-\alpha}} \quad (12)$$

The equivalent stress $\bar{\sigma}$ is given by the adapted Norton-Hoff behavior law. As discussed in [1], the evolution of $\bar{\sigma}$ with the strain path β is simpler to use in a finite element code. These diagrams are defined as Extended Scattering Forming Limit Stress Diagram (ESFLSD). Figs 21 show the evolution of the critical equivalent stress, defined as a function of the strain path as developed in [13]. The strain rate increases dramatically the values of the critical stresses as seen in Tab. 11. The extremum values obtained for the tensile test and the equibiaxial ($\beta = 1$) are sufficient to reconstruct the limit curves because the standard deviations are not so dispersive (it varies from 2 MPa to 9 MPa) as shown in Tab. 12 and dramatically limit the experimental tests.

	Tensile tests				**Bulge test - Elliptical**		**Bulge test - Intermediate**		**Bulge test - Circular**	
Strain rate (s^{-1})	0.008	0.15	1.5	4.5	0.01	0.15	0.01	0.15	0.01	0.15
0°	223.5	284.7	343.1	368.1	224.1	291.3	231.5	297.7	225.2	290.5
45°	239.6	308.3	381.3	405.3	239.3	312.9	246.6	320.7	249.1	325.8
90°	278.1	335.8	377.9	403.6	273.9	331.3	286.1	344.6	297.9	361.1

TABLE 11: Mean values of the equivalent critical stresses (MPa)

	Tensile tests				**Bulge test - Elliptical**		**Bulge test - Intermediate**		**Bulge test - Circular**	
Strain rate (s^{-1})	0.008	0.15	1.5	4.5	0.01	0.15	0.01	0.15	0.01	0.15
0°	3.72	2.45	3.4	4.79	3.75	2.2	4.49	2.83	3.9	3.25
45°	4.82	4.53	8.03	9.14	4.77	2.99	5.31	3.92	5.4	3.5
90°	5.15	5.51	5.46	5.88	5	4.7	5.07	4.37	5.49	4.62

TABLE 12: Standard deviation related to the equivalent critical stresses (MPa)

This definition of the critical stresses can directly be used in a FE software to define failure criterion as described in [1] and it will be the next step of this work.

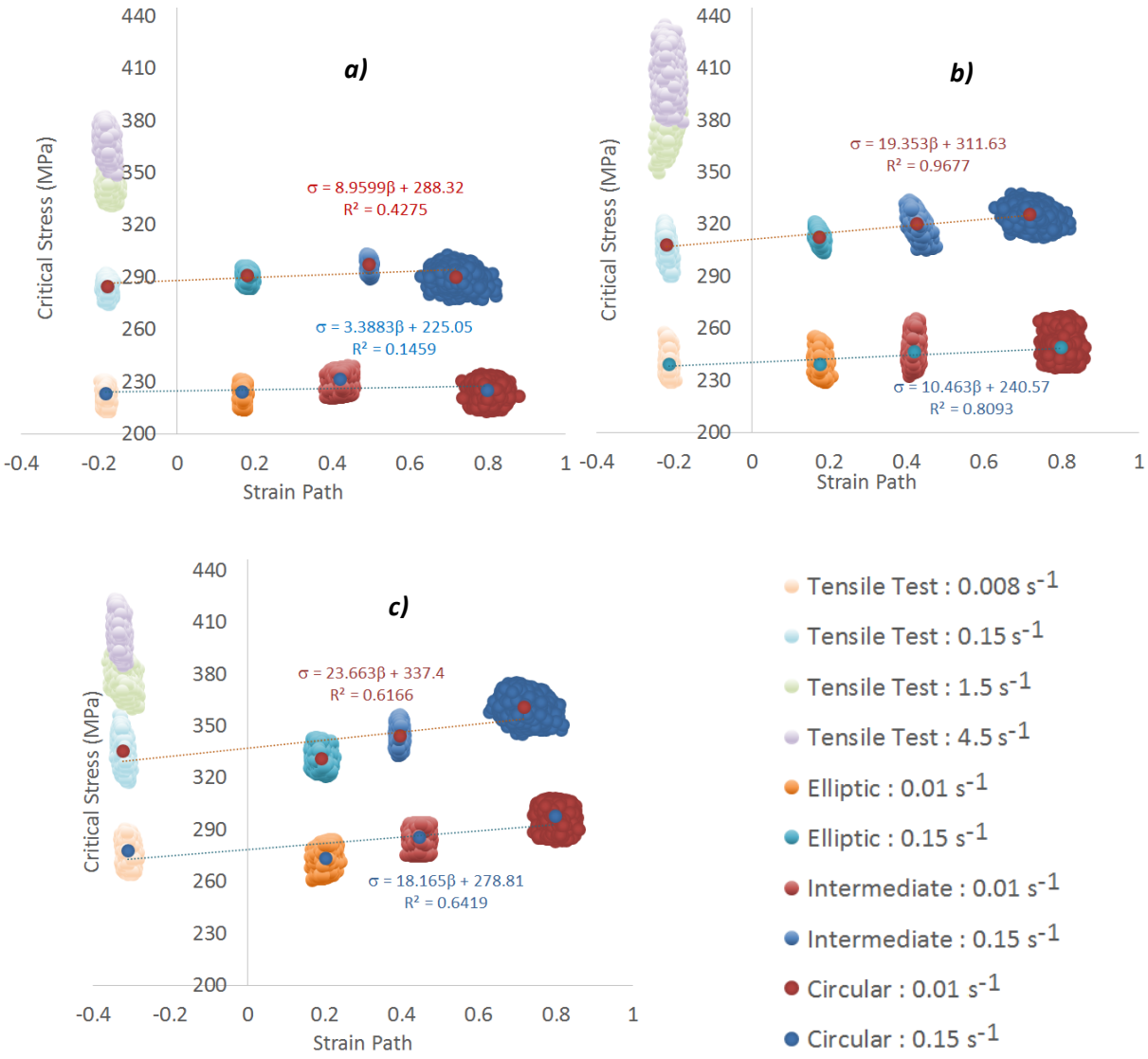

FIGURE 21: Extended Scattering Forming Limit Stress Diagram (ESFLSD) in the *a*) 0°; *b*) 45° and *c*) 90°

Conclusion

Several experimental tests were carried out to assess the scattering of material parameters all along the primary coil of zinc alloy. The goal was to estimate the scattering along the width of the coil and along the length. The variation of the values in the width and the length of the coil is not significant for all material parameters identified by the GRG method. However, the scattering is important and seems increasing with the velocity as shown in Figs. 3 and 4 and the hardening coefficient values increase with strain rate. The entire SFLD indicates that the role of the strain rate on the evolution FLCs is minor.

Conflict of Interest: The authors declare that they have no conflict of interest.

References

1. Milesi M, Logé RE, Pino-Muñoz D, Jansen Y, Bouchard PO (2017) Accounting for material parameters scattering in rolled zinc Formability. J. Mat. Process. Tech. 245:134-148

2. Diot M, Philippe MJ, Wégria J, Esling C (1999) Texture gradient in rolled zinc sheets. Scripta Mater. 40 (11):1295-1303

3. Pantazopoulos G, Toulfatzis A, Vazdirvanidis A, Rikos A (2017) Fundamental aspects of rolled Zn alloy sheet formability: structure-property and failure mode relationships. Mat. Sci. Forum, Trans Tech Publications 879:1443-1448

4. Schlosser F, Schwindt C, Fuster V, Tommasi A. Signorelli JW (2017) Crystallographic texture evolution of a zinc sheet subjected to different strain paths. Metall. and Mat. Trans. A 48 (6):2858-2867

5. Milesi M, Logé RE, Jansen Y (2014) Anisotropic behavior and formability criterion for zinc sheets. J. of Mat. Process. Tech. 214:2869-2876

6. Khachiyan L (1979) A polynomial algorithm in linear programming. Doklady Akademiia Nauk SSSR:1093–1096

7. Box GEP, Müller ME (1958) A note on the generation of random normal deviates. Annals of Mathematical Statistics 29:610-611

8. Keeler SP, Backhofen WA (1964) Plastic instability and fracture in sheet stretched over rigid punches. ASM Transaction 56:25-48

9. Haberfield AB, Boyles MW (1973) Laboratory determined forming limit diagrams. Sheet Met. Ind, 50:400-405 & 411

10. Candau N, Pradille C, Bouvard JL, Billon N (2016) On the use of a four-cameras stereovision system to characterize large 3D deformation in elastomers. Polymer Testing 56:314-320

11. Lasdon LS, Fox RL, Ratner MW (1973) Nonlinear Optimization Using the Generalized Reduced Gradient Method. Technical Memorandum 325, NTIS

12. Jansen Y (2013) Modélisation et optimisation du processus de formage de pièces en zinc. PhD, MinesParistech, Sophia-Antipolis, France

13. Arrieux R, Bedrin C, Boivin M (1982) Determination of an intrinsic forming limit stress diagram for isotropic metal sheets. Proceedings of the 12th Biennal Congress of the IDDRG:61-71

14. Matsumoto M, Nishimura T (1998) Mersenne twister, a 623-dimensionnally equidistributed uniform pseudorandom number generator. ACM Transactions on Modelling and Computer Simulations 8:3-30

15. Paul SK (2015) Path independent limiting in sheet metal forming. J. of Manufact. Process 20:292-303